Marangoni convection in droplets on superhydrophobic surfaces

By DANIEL TAM[1], VOLKMAR von ARNIM[2] †, G. H. McKINLEY[2] AND A. E. HOSOI[2]

[1]Department of Aeronautics and Astronautics, Massachusetts Institute of Technology, 77 Massachusetts Avenue, Cambridge, MA 02139, USA

[2]Hatsopoulos Microfluids Laboratory, Department of Mechanical Engineering, Massachusetts Institute of Technology, 77 Massachusetts Avenue, Cambridge, MA 02139, USA

(Received ?? and in revised form ??)

We consider a small droplet of water sitting on top of a heated superhydrophobic surface. A toroidal convection pattern develops in which fluid is observed to rise along the surface of the spherical droplet and to accelerate downwards in the interior towards the liquid/solid contact point. The internal dynamics arise due to the presence of a vertical temperature gradient; this leads to a gradient in surface tension which in turn drives fluid away from the contact point along the interface. We develop a solution to this thermocapillary-driven Marangoni flow analytically in terms of streamfunctions. Quantitative comparisons between analytical and experimental results are presented as well as effective heat transfer coefficients.

1. Introduction

Non-wettability, effective heat transfer coefficients and other material properties of hydrophobic surfaces are of interest in many industrial applications, such as efficient condensing design and waterproofing textiles. Since Wenzel (1936) noted seventy years ago that the hydrophobicity of a substrate can be enhanced through a combination of chemical modification and surface roughness, multiple studies have observed a substantial increase in static contact angles by integrating these two strategies. More recently the non-wetting properties of these substrates have been further enhanced and contact angles close to 180° have been achieved by introducing nanoscale roughness (e.g. Quéré 2002; Bico *et al.* 1999; Zhao *et al.* 2005).

Numerous techniques have been developed over the past decade for fabricating robust superhydrophobic surfaces by combining chemical non-wetting treatments with controllable levels of roughness over a wide range of length scales. General discussions of the principles for preparing such surfaces are given by Quéré (2003) and by Otten & Herminghaus (2004). Onda *et al.* (1996) and co-workers used fractal patterns formed in an alkene wax to produce the first superhydrophobic surfaces with contact angles greater than 160°. Since then surfaces have been prepared using a variety of materials processing techniques including: lithographically patterned silicon posts having a wide range of aspect ratios (Lafuma & Quéré 2003; Krupenkin *et al.* 2004); silicone arrays patterned using soft lithography (He *et al.* 2003); layer-by-layer (LBL) assembled polymeric coatings decorated with nanoparticles (Zhai *et al.* 2004); and microporous polymeric silica structures (Gao & McCarthy 2006) in addition to the vertically aligned carbon nanotube

† Present address: ITV Denkendorf, Koerschtalstr. 26, 73770 Denkendorf, Germany

Heat Transfer via Phase Change on Hydrophobic Surfaces

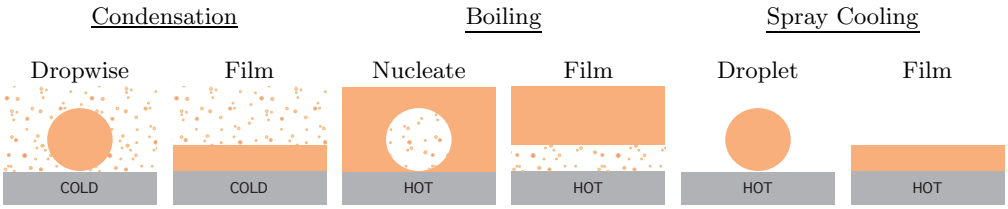

Erb & Thelen (1965)	N/A	Kandlikar (2001) Thomas *et al.* (2003)	Present Study	N/A

Table 1. Summary of heat transfer in various geometries from superhydrophobic surfaces. A few representative studies are listed in each regime.

carpets (Lau *et al.* 2003) used in the present study. In many of these formulations the surface coating consists of polymeric or ceramic constituents that are poor thermal conductors which limits the efficacy of the surface in heat transfer applications. One of the advantages of the carbon nanotube carpets employed in the present work is the high axial thermal conductivity of the graphene sheets that form the multiwall nanotubes.

Heat transfer properties of hydrophobically modified surfaces have primarily been studied in the context of condensation on cooled substrates (see Table 1). In most applications, dropwise condensation is preferable to film condensation as the continuous condensed fluid film acts as an insulating layer, resulting in lower heat transfer coefficients (Schmidt *et al.* 1930). Thus it is often advantageous to promote dropwise condensation by changing the wettability of the relevant surfaces, making them hydrophobic (e.g. Erb & Thelen 1965). Recent studies have taken this one step further; by introducing wettability gradients into the substrate, condensing drops rapidly move towards more hydrophilic regions providing a passive mechanism that can increase the effective heat transfer coefficient by an order of magnitude (Daniel *et al.* 2001).

The reverse problem of a liquid impinging on a hot surface has been less well-studied in the context of hydrophobic surfaces though numerous articles exist describing the evaporation of a single drop on a partially wetting substrate (e.g. Deegan *et al.* 1997; Makino *et al.* 1984; Sadhal & Plesset 1979) and extensive studies have been performed on the Leidenfrost effect (see e.g. recent work by Biance *et al.* 2003). It has also been demonstrated that the effective heat transfer in such droplet systems can be significantly enhanced by adding surfactant to the fluid, decreasing the contact angle, and promoting nucleation within the impinging droplet (Jia & Qiu 2002; Qiao & Chandra 1997). One of the few studies that incorporates the effects of hydrophobicity is McHale *et al.* (2005) in which a slowly evaporating droplet on a patterned polymer surface was investigated. Unlike our system, the substrate was not heated and hence the droplet remained in a parameter regime in which Marangoni stresses were negligible.

In addition, a limited number of studies have investigated the effects of surface chemistry on boiling. Wang & Dhir (1993) conducted an experimental study to quantify the effects of surface wettability on the density and distribution of nucleation sites. They confirmed that increasing wettability both shifts the boiling curve to the right and increases the maximum heat flux, and found that the fraction of cavities that nucleate decreases as the wettability of the surface improves. Kandlikar (2001) presents a nice

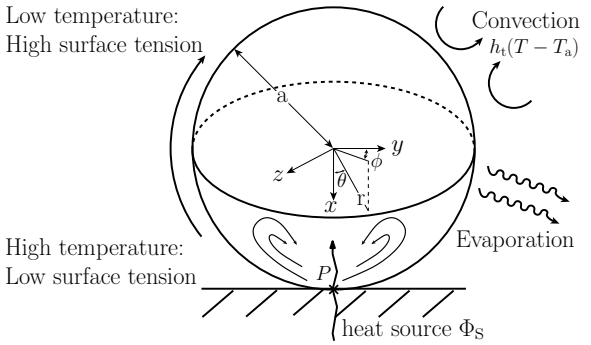

FIGURE 1. Schematic and notation for a droplet on a superhydrophobic surface.

review and brief history of the study of pool boiling. The author then goes on to derive a mathematical model to predict critical heat fluxes which account for the effects of hydrophobicity (through changes in the static contact angle), vapor momentum and gravity. Predictions from this model are successfully compared with existing experimental data. More recently, Thomas *et al.* (2003) performed an experimental study in which the authors applied short microsecond voltage pulses to investigate the effect of surface properties on fast, transient microboiling.

However, the full problem of understanding the heat and mass transfer properties of a single stationary droplet on a heated hydrophobic surface is further complicated by the presence of a mobile free surface. Gradients in temperature along the free surface lead to gradients in surface tension which may in turn drive thermocapillary Marangoni convection (Marangoni 1865) within the drop (as illustrated in Figure 1). A detailed and extensive literature on thermocapillary driven flows exists and both experimental and theoretical studies are reviewed in Schatz & Neitzel (2001) and Davis (1987) respectively, and in Subramanian & Balasubramaniam (2001) which considers thermocapillary motion in droplets and bubbles.

One of the few analyses that has carefully investigated the effects of Marangoni stresses in evaporating sessile drops is the recent study by Hu & Larson (2005). In this work, the authors model convection in a droplet on a partially wetting surface using both a lubrication analysis and a full finite element model (FEM). They find that convection rolls are observed – with a down-welling in the center of the droplet – driven by a nonuniform temperature distribution at the surface of the droplet which arises from evaporative cooling. Surprisingly, the lubrication approximation is in good agreement with the FEM even for contact angles as high as 40°.

In this study, we investigate Marangoni convection within a single droplet on a heated superhydrophobic surface. The analysis differs from that of Hu & Larson (2005) in that our droplet is nearly spherical and hence not amenable to lubrication techniques. Ultimately, by comparing experimental data with analytic predictions, we can extract a value for the effective heat transfer coefficient of the system. In §2 we describe the experimental setup and procedure. In §3 we derive the governing equations for the system which are then solved analytically in §4. Section 5 presents a quantitative comparison of analytic and experimental results.

2. Experimental setup

A schematic of the experimental setup is shown in Figure 2. Monodisperse silica particles 300 nm in diameter were added to deionized water at a concentration of 1wt% in

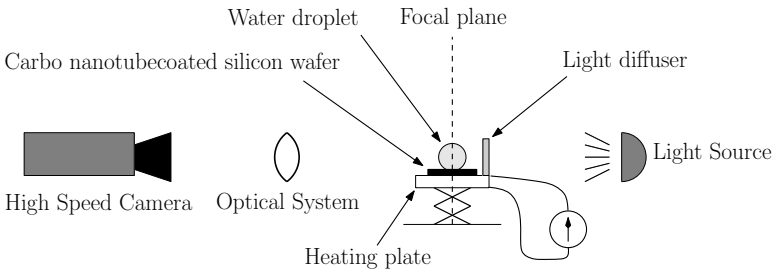

FIGURE 2. Schematic of the experimental setup.

order to track convective motions (see Figure 3). The droplets were formed at the tip of a thin glass capillary approximately 10 μm in diameter, and were deposited on a silicon wafer coated with a vertically aligned carpet of carbon nanotubes (for details on the non-wetting properties and manufacture of the superhydrophobic surface see Lau *et al.* 2003). The radii of the droplets ranged between $0.4 - 0.6$ mm and contact angles were near 180° (see Figure 3a). The superhydrophobic surface was heated from below via a heating plate with variable input current.

As soon as the liquid droplet is put in contact with the heated surface, the fluid is set in motion and convective structures develop. In order to visualize the temperature and velocity fields, both optical and infrared images of the droplet were taken. Figure 3(b) is a thermal image of the droplet taken with a FLIR Systems ThermaCAM infrared camera, which reveals a temperature gradient inside the droplet that is roughly oriented towards the contact point. The maximum temperature variation within the drop ranged from approximately $1 - 20$°C and the temperature of the substrate did not exceed 50°C. Particle paths were visualized using a Phantom HSV v5.0 high speed camera at 400 fps in conjunction with a long-distance video microscope system (K2 Infinity). The droplets were illuminated from behind with a diffuse light source, as represented in Figure 2. The image is focused on the thin glass capillary, which corresponds to the midsection of the droplet. The local velocity field within the droplet was measured by tracking small solid particles within the focal plane at the center of the droplet (see Figure 3c). Particles within the focal plane appear as sharp points – although some residual blurry images of particles that are close to, but out of, the focal plane remain in the image. Typical velocities of the inner flow near the center of the droplet were measured to be approximately $u_{\mathrm{meas}} \approx 1$ mm s^{-1} and the characteristic time scale for one complete cycle of the convective structures was on the order of 1 s. Particle velocities were observed to increase significantly in the vicinity of the heat source (by at least an order of magnitude). At the surface of the droplet, the fluid is convected upwards, away from the heat source. In the focused midsection of the droplet, particles are accelerated downwards, away from the free surface towards the contact point P (see Figure 1 for notation). Also, particles that are initially out of the plane of focus are observed to move towards the focal plane and the contact point P. This suggests an axisymmetric toroidal geometry for the convective structures. Data was recorded for various values of heat input and drop size.

On a clean carbon nanotube surface, the convective structures are observed to reach a stable steady state. However, the observed structures are extremely sensitive to the substrate properties. As particles left by previous experiments accumulated on the substrate, the quality of the surface degraded and the stability of the observed convection rolls declined. After several seconds the structures became unstable ultimately culminating in an unstructured swirling of the entire droplet. Owing to the extreme sensitivity of the

	Symbol	Value
Gravity	g	$9.8\ \mathrm{m\ s^{-2}}$
Density of water	ρ	$9.982 \times 10^{2}\ \mathrm{kg\ m^{-3}}$
Dynamic viscosity of water	μ	$1.002 \times 10^{-3}\ \mathrm{kg\ m^{-1}s^{-1}}$
Kinematic viscosity of water	ν	$1.004 \times 10^{-6}\ \mathrm{m^2\ s^{-1}}$
Specific heat of water	C_p	$4.182 \times 10^{3}\ \mathrm{J\ kg^{-1}K^{-1}}$
Thermal conductivity of water	k_w	$5.9 \times 10^{-1}\ \mathrm{W\ m^{-1}K^{-1}}$
Thermal conductivity of air	k_air	$2.4 \times 10^{-2}\ \mathrm{W\ m^{-1}K^{-1}}$
Thermal diffusivity of water	κ	$1.41 \times 10^{-7}\ \mathrm{m^2\ s^{-1}}$
Coefficient of thermal expansion	α_t	$3.0 \times 10^{-4}\ \mathrm{K^{-1}}$
Change in surface tension due to temperature	$\alpha = \partial\sigma/\partial T$	$-0.155 \times 10^{-3}\ \mathrm{kg\ s^{-2}K^{-1}}$
Latent heat of vaporization	L_v	$2.454 \times 10^{6}\ \ \mathrm{J\ kg^{-1}}$
Saturation temperature at atmospheric pressure	T_s	373 K
Atmospheric temperature	T_a	~ 295 K
Characteristic radius of the droplets	a	$\sim 0.5 \times 10^{-3}$ m

TABLE 2. Characteristic values of relevant physical parameters.

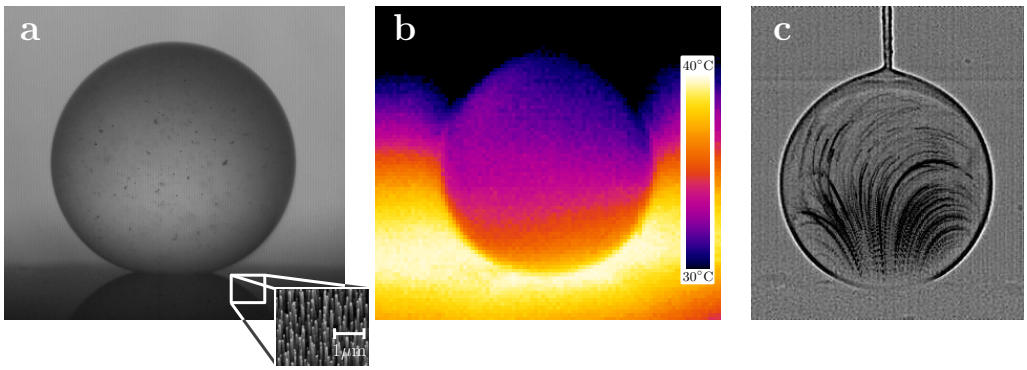

FIGURE 3. a) Photo of a water droplet (0.5 mm radius) on a superhydrophobic surface seeded with silica tracer particles. The inset shows an SEM image of the surface coated with a carbon nanotube forest. b) Thermal image of a drop deposited on the heated substrate showing contours of constant temperature. c) Superposition of 20 consecutive snapshots of the water droplet taken at 10 ms time intervals, showing the inner convective motion of the fluid. Particles are moving downward in the center of the droplet. The "stem" at the top of the droplet is the glass capillary that was used to deposit the droplet. The capillary was removed before any data was recorded. It bears emphasis that for illustration purposes, images (b) and (c) were taken using larger values of heat flux and brighter lightning than those used in data collection. In later experiments, the temperature at the heating plate was lowered in order to remain in the stable roll regime, and the light source was dimmed to avoid thermal contamination.

convection pattern to the quality of the substrate, all the experimental data presented herein was taken on a clean, freshly-prepared surface.

3. Physical model

Consider a liquid of dynamic viscosity μ, density ρ, thermal conductivity k_w, specific heat C_p, saturation temperature T_s and latent heat of vaporization L_v. We assume that the carbon nanotube surface heats the liquid droplet of radius a at the contact point P and we neglect any radiative heat transfer. There are at least three possible mechanisms that could drive convection in the droplet: buoyant convection, Marangoni (surface

tension-driven) convection, or mass flow arising from a pinned contact line coupled with spatially nonuniform evaporation, as in the "coffee stain" problem (Deegan *et al.* 1997). As our experiments are performed on a superhydrophobic surface, the contact line is free to move and we can rule out the coffee ring phenomenon. Hence we consider the possibility of Marangoni and/or buoyant convection. Note that both are theoretically possible as the temperature inside the droplet increases locally near the contact point creating a temperature gradient directed towards P. Since the surface tension (and density) of water increases as the temperature decreases, this temperature gradient generates both a gradient in surface tension at the interface, which drives the fluid upwards at the surface of the droplet, and a gradient in density which represents an unstable configuration with heavy fluid on top of light fluid.

In our experiments there is palpable evidence that the driving mechanism cannot be buoyancy as the rolls are going in the wrong direction – with a down-welling in the center of the droplet and an upflow at the interface. However, despite this clear indication of Marangoni convection, as observed by Scriven & Sternling (1964), "because flows actually powered by ... interfacial tension have been overlooked or misconstrued so often, there seems to be a need for simple criteria by which they can be recognized." In light of this prevalent misconception, it is worth examining in some detail under what conditions we expect to see Marangoni flows in our droplets.

The Rayleigh number $\mathrm{Ra} = \alpha_t g a^3 \Delta T / \nu\kappa$ – which determines stability in buoyant convection – is roughly 50 in our experiment. For reference, the critical Rayleigh numbers characterizing the onset of buoyancy-driven instabilities are typically on the order of 10^3 depending on the geometry; for convection between two flat plates, the critical Rayleigh number is 1707, for a sphere under radial gravity it is 3091 (Chandrasekhar 1961). Judging by these typical numbers one might be tempted to speculate that a Rayleigh number of 50 would place our droplet well into the stable regime. However, some care must be taken as these critical values depend on the geometry of the system. In our case, since there are regions in which the direction of the tangent to the free surface aligns with the direction of gravity, the flow is more prone to instability. Hence, in the following we perform a scaling analysis to determine under what conditions we expect to observe Marangoni convection in our particular geometry.

3.1. *Scaling*

Both the Rayleigh number and the Marangoni number can be interpreted as a ratio of time scales: namely the ratio of the characteristic time scale associated with thermal diffusion which stabilizes the flow, $\tau_{diff} \sim a^2/\kappa$, to the characteristic time scale associated with convection. In our analysis we will denote these convective time scales as τ_B for flows driven by density gradients and τ_M for flows driven by surface tension gradients. If the stabilizing diffusive time scale is short compared to τ_M and τ_B, i.e. if the dimensionless quantities $\mathrm{Ma} \equiv \tau_{diff}/\tau_M$ and $\mathrm{Ra} \equiv \tau_{diff}/\tau_B$ are small, the system in stable and there is no convection. Similarly, if the system is unstable, we expect Marangoni convection to be dominant if $\mathrm{Ma}/\mathrm{Ra} = \tau_B/\tau_M$ is large and buoyant convection to be dominant if this ratio is small. To determine which of these is the principal effect in our system, we need to estimate τ_B and τ_M for our particular geometry.

The characteristic velocity of Marangoni flows scales like $U_M \sim \alpha\Delta T/\mu$ (see e.g. Equation (4.2)). To find the characteristic velocity associated with buoyant convection, we balance the rate of viscous dissipation within the roll with the rate at which potential energy is gained as the heavier fluid descends:

$$\int \mu \nabla(\mathbf{u})^2 dV \sim \Delta\rho g U_B a^3. \tag{3.1}$$

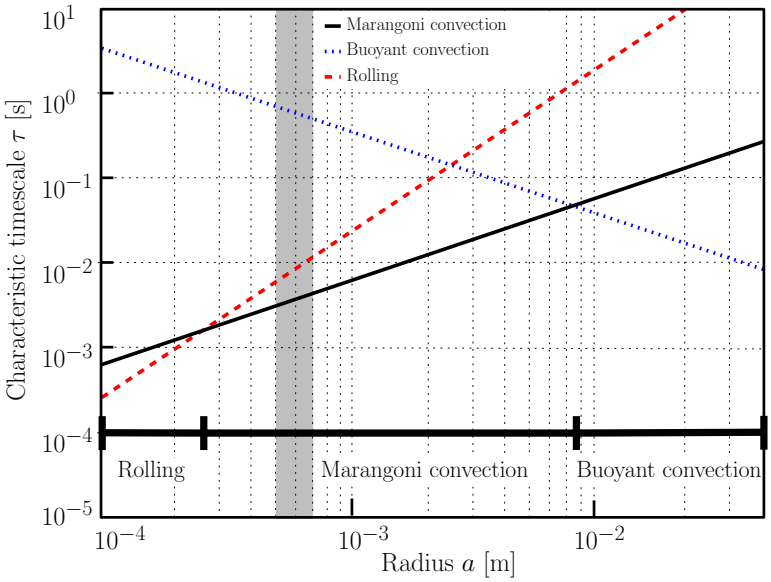

FIGURE 4. Characteristic convective timescales for various sizes of water droplets. The grey shaded region indicates the range of droplet sizes in our experiments. Material parameters correspond to those of water with $\Delta T = 1°\mathrm{C}$. Note that, as all three curves scale linearly with ΔT, changing the temperature difference does not change the radius at which the curves intersect – rather it rescales the vertical axis.

The integral on the left scales as $\mu(U_B/a)^2a^3$, hence the characteristic velocity associated with buoyancy-driven convection is $U_B \sim \Delta\rho g a^2/\mu$. This velocity can be also written as $U_B \sim \alpha_t \rho g a^2 \Delta T/\mu$ with $\Delta\rho \sim \alpha_t \rho \Delta T$. As discussed above, in general, the instability with the fastest growth rate, or shortest characteristic time scale, will be the one that is observed. Using our estimates for typical velocities associated with Marangoni and buoyant convection, we can estimate the ratio of convective time scales:

$$\frac{U_M}{U_B} \sim \frac{\tau_B}{\tau_M} \sim \frac{\alpha \Delta T}{\Delta \rho g a^2} \sim \frac{\alpha}{\alpha_t \rho g a^2}. \tag{3.2}$$

It bears emphasis that this ratio of time scales corresponds to the ratio of the Marangoni number over the Rayleigh number $\tau_B/\tau_M = \mathrm{Ma}/\mathrm{Ra}$, with $\mathrm{Ra} = \alpha_t g a^3 \Delta T/\nu\kappa$ and $\mathrm{Ma} = \alpha a \Delta T/\kappa\mu$. As with convection in thin films, we expect to observe Marangoni convection at small length scales (i.e. in thin films and small drops) and buoyant convection for larger length scales (thicker layers and larger drops) (Scriven & Sternling 1964). For water, the transition to buoyancy-dominated convection occurs around $a \gtrsim 1$ cm which is considerably larger than the droplets in our experiment.

However, this is not the whole story. Although we are far from the onset of buoyancy-driven convection in our experiments, there is another buoyancy-driven instability that one might expect to observe. Namely, as the fluid is heated from below, and cooled from above, we have the inherently unstable situation of a sphere with its center of mass above its geometric center – hence, the droplet should roll. For a sphere, this instability should manifest for arbitrarily small Rayleigh numbers. In our experiments, we are saved from this complication because, in the neighborhood of the contact point, the sphere is slightly deformed giving the droplet a stabilizing base. The extent and effectiveness of this finite size contact region can be calculated following the arguments of Mahadevan & Pomeau (1999), who found that the size of the contact region, ℓ, scales like the inverse Capillary

number, ℓ_C, namely:

$$\ell \sim \frac{a^2}{\ell_C} = a^2\sqrt{\frac{\rho g}{\sigma}}\ . \tag{3.3}$$

Again, the characteristic velocities and time scales associated with rolling can be computed by balancing the rate of potential energy gained by rolling with the rate of viscous dissipation. In this case, the viscous dissipation is restricted to the deforming contact region (as the rest of the drop is in solid body rotation):

$$\iiint \mu\nabla(\mathbf{u})^2 dV \sim \mu\left(\frac{U_R}{a}\right)^2 \ell^3 \sim \Delta\rho g U_R a^3. \tag{3.4}$$

Hence the characteristic velocity associated with rolling, U_R, is given by $U_R \sim \Delta\rho g\ell_C^3/(\mu a)$. Comparing the time scale associated with the onset rolling with that of buoyancy-driven convection, we find:

$$\frac{\tau_R}{\tau_B} \sim \frac{U_B}{U_R} \sim \frac{a^3}{\ell_C^3} = \mathrm{Bo}^{\frac{3}{2}} \tag{3.5}$$

where Bo is the Bond number. Hence, rolling will manifest at small Bond numbers.

All three time scales are summarized in Figure 4 where the material parameters have been chosen for water. As one can see from the figure we expect to see transitions between the three types of instabilities as one varies the radius of the droplet. For very small drops, we expect to see rolling ($a \ll 0.3$ mm). This is consistent with our experimental observations as very tiny droplets either roll off the apparatus or, if they are pinned with a pipet, exhibit large swirling motions on the scale of the droplet. For droplet sizes ranging between 0.3 mm $\ll a \ll 7$ mm, we expect to observe Marangoni convection – namely toroidal convection rolls flowing inward. This is what was observed in the bulk of our experiments. Finally, for very large droplets ($a \gg 7$ mm) we expect to see a transition to buoyant convection. This parameter range was outside our regime of interest as the "droplets" are considerably larger than the Capillary length and deviate from the spherical geometry assumed herein. Hence we restricted our experimental data to droplets below this transition.

3.2. *Governing equations*

Having established that Marangoni convection is the dominant instability within the parameter regime represented in our experiments, we present a model for conservation of momentum and energy, subject to the relevant boundary conditions, that incorporates the first order effects of surface tension gradients. In this analysis, we consider the small Reynolds number limit and neglect inertial effects within the drop†. Thus, the governing equations for the fluid motion are the incompressible Stokes equations:

$$\boldsymbol{\nabla} p = \mu\boldsymbol{\nabla}^2\mathbf{u}, \qquad \boldsymbol{\nabla}\cdot\mathbf{u} = 0 \tag{3.6}$$

where p and $\mathbf{u}$ are the pressure and velocity fields within the droplet respectively.

† Some care must be taken in defining the Reynolds number as the velocity varies considerably within the droplet owing to the mathematical singularity at the point of contact where both the temperature field and velocity field diverge. In this small region, neither the Péclet number, Pe, nor the Reynolds number is small. Elsewhere (in more than 99% of the volume of the droplet), the flows are slow and inertia is negligible (Re $\ll 1$) in both the experiment and in the analytical solution. If the neighborhood in which Re becomes significant is sufficiently small, we expect the model to capture the experimentally observed structures reasonably well away from the point of contact; however, one cannot expect the model to accurately reflect the behaviour of the flow in the neighborhood of the singularity. In reality, this singularity is mitigated by the finite extent of the contact region; estimates for the size of this region are discussed in section 3.1.

The governing equation for the heat transfer problem is given by conservation of energy

$$\rho C_{\mathrm{p}} \left(\frac{\partial T}{\partial t} + \mathbf{u} \cdot \boldsymbol{\nabla} T \right) = k_{\mathrm{w}} \boldsymbol{\nabla}^2 T + \phi - \Phi_{\mathrm{s}} \delta(\mathbf{r} - \mathbf{r}_0) \ , \tag{3.7}$$

where ϕ is the viscous dissipation per unit volume and T is the temperature field within the droplet. In equation (3.7), the heat conduction term scales as $k_{\mathrm{w}} \Delta T / a^2 \approx 10^6$ for a characteristic temperature difference inside the droplet of about 10K. On the other hand, the viscous dissipation term scales as $\mu {u_{\mathrm{meas}}}^2 / a^2 \approx 10^{-3}$ and is therefore negligible relative to conduction. In this simple system, heat exchange takes a number of different forms – convection, conduction, and evaporation – at the boundary as summarized in Figure 1. The small region of contact between the hydrophobic surface and the droplet is modeled as a point heat source†. We thus include a delta function at the contact point of intensity Φ_{s}, where Φ_{s} has units of J s^{-1} and $\mathbf{r_0}$ is the vector postion of the contact point. Altenatively, the three-dimensional delta function $\delta(\mathbf{r} - \mathbf{r}_0)$ in equation (3.7) can be written as $\delta(\mathbf{r} - \mathbf{r}_0) = \delta(|\mathbf{r} - \mathbf{r}_0|)/4\pi|\mathbf{r} - \mathbf{r}_0|^2$.

Using values from Table 2, the characteristic time scales for heat advection and diffusion are given by

$$t_{\mathrm{diff}} = \frac{\rho C_{\mathrm{p}} a^2}{k_{\mathrm{w}}} \approx 1 \text{ s} \ , \qquad t_{\mathrm{adv}} = \frac{a}{u_{\mathrm{meas}}} \approx 1 \text{ s} \ . \tag{3.8}$$

In our experimental observations, the vortex structure was observed to be stable for at least 60 s. Thus, the convection rolls can reasonably be assumed to be a steady state phenomenon over the time scale of the experiment and we neglect the time dependency in the energy equation.

The Péclet number, Pe, can be written as the product of the Reynolds number, Re, and the Prandlt number, Pr:

$$\mathrm{Pe} = \mathrm{Re} \cdot \mathrm{Pr} \ . \tag{3.9}$$

Although not rigorously negligible throughout the entire domain in the experiments, the convective effects scale with Re as the Prandtl number is constant for a given fluid; for water, $\mathrm{Pr} = \mu C_{\mathrm{p}} / k_{\mathrm{w}} \approx 7.2$. Therefore, the Péclet number is considered small in the following analytical study (to be consistent with the small Reynolds number assumption above), and diffusion is considered to be the major mode of heat transfer inside the droplet‡. Thus the governing heat equation reduces to Poisson's equation for the temperature field:

$$k_{\mathrm{w}} \boldsymbol{\nabla}^2 T = \Phi_{\mathrm{s}} \frac{\delta(|\mathbf{r} - \mathbf{r}_0|)}{4\pi|\mathbf{r} - \mathbf{r}_0|^2} \ . \tag{3.10}$$

3.3. *Boundary conditions*

At the surface of the droplet both heat transfer, via convection and conduction to the surrounding air, and evaporation tend to cool down the droplet. The convective and conductive heat transfer at the interface between the water droplet and the surrounding air is modeled with Newton's law of cooling (e.g. Incropera & deWitt 2002), which can be written as

$$\phi_{\mathrm{t}} = h_{\mathrm{t}} (T - T_{\mathrm{a}}) \ , \tag{3.11}$$

where ϕ_{t} is the total heat flux due to convection and conduction, h_{t} is the heat transfer coefficient and T_{a} is the ambient temperature.

† Appendix C investigates the effect of the point heat source assumption on the solution.

‡ The effects of finite Péclet number are explored in Appendix D.

The local energy loss due to evaporation can be written as

$$\phi_{\text{evaporation}} = J\left[C_{\text{p}}(T - T_{\text{s}}) + L_{\text{v}}\right] \ , \tag{3.12}$$

where J is the local mass flux due to evaporation. In our case $T - T_{\text{s}} \approx 60\text{K}$, thus $C_{\text{p}}(T - T_{\text{s}}) \approx 10^5$ J kg^{-1} and $L_{\text{v}} \approx 10^6$ J kg^{-1}. Therefore, we neglect the first term in equation (3.12) and assume that the latent heat of vaporization does not depend on temperature. The local mass flux J depends on a number of variables including the temperature at the interface T, the pressure at the interface p, the relative humidity of the air H_{m}, and the local curvature R^{-1}. Over the time scale of the convective structure p, H_{m} and R^{-1} are all constant, and J can be written as a function of the local temperature T only. For small temperature differences, the mass flux J can be safely approximated as a linear function of T. Recall that the temperature is a function of position, $T = T(\mathbf{r})$, and hence the first-order effects of the geometry of the droplet are accounted for via the temperature field.

Combining the two terms ϕ_{t} (3.11) and $\phi_{\text{evaporation}}$ (3.12), the energy flux boundary condition at the surface of the droplet takes the form

$$-k_{\text{w}}\boldsymbol{\nabla} T\cdot\mathbf{n} = h(T - T_0) \ , \tag{3.13}$$

where h is the effective total heat transfer coefficient, $\mathbf{n}$ is the unit vector normal to the interface and T_0 is a reference temperature. Because the equation is linear in the temperature T, the reference temperature, T_0, can be scaled out of the problem and does enter into our calculation.

The boundary conditions for Stokes equations (3.6) correspond to a stress balance at the surface of the droplet projected in the normal and tangential directions. The normal stress balance is replaced by the assumption that the droplet remains spherical. This assumption is experimentally satisfied because the Bond number, characterizing the ratio of gravity over surface tension, is small ($\text{Bo} = \rho g a^2/\sigma \ll 1$) and because of the non-wettability of the substrate. The tangential stress balance can be written as follows:

$$\mathbf{t}\cdot\boldsymbol{\pi}\cdot\mathbf{n} = \mathbf{t}\cdot\boldsymbol{\nabla}_{\text{s}}\sigma \tag{3.14}$$

where $\boldsymbol{\pi}$ is the stress tensor, $\mathbf{t}$ is the unit vector tangent to the interface, $\boldsymbol{\nabla}_{\mathbf{s}}$ is the gradient along the surface and $\sigma = \sigma(T)$ is the surface tension. Thermocapillary effects arise due to gradients in surface tension, which again may be approximated as linear in temperature such that

$$\sigma = \sigma_{\text{a}} - \alpha\cdot(T - T_{\text{a}}) \ , \tag{3.15}$$

where σ_{a} is the surface tension at ambient temperature, T_{a}, and α is the first derivative of the surface tension with respect to the temperature at T_{a}.

4. Analytical solution

The assumption that the Péclet number is small decouples the energy conservation equation from the Stokes equations (3.6). Therefore, (3.10) is solved first using the boundary condition (3.13). Equation (3.6) is then solved by introducing the previously obtained solution for the temperature field in the boundary condition (3.14).

4.1. *Nondimensionalization*

The problem is nondimensionalized as follows:

$$\widetilde{\mathbf{r}} = \mathbf{r}/L_{\text{ref}}, \quad \widetilde{\mathbf{u}} = \mathbf{u}/u_{\text{ref}}, \quad \widetilde{p} = p/p_{\text{ref}}, \quad \widetilde{T} = (T - T_0)/\Delta T_{\text{ref}} \ , \tag{4.1}$$

using the scales

$$L_{\rm ref} = a, \quad \Delta T_{\rm ref} = \Phi_{\rm s}/4\pi k_{\rm w} a, \quad u_{\rm ref} = |\alpha|\Delta T_{\rm ref}/\mu, \quad p_{\rm ref} = \mu u_{\rm ref}/a, \tag{4.2}$$

where $\Delta T_{\rm ref}$ is the characteristic temperature variation induced by a point heat source of intensity $\Phi_{\rm s}$ and is obtained directly from the nondimensionalization of equation (3.10), and $u_{\rm ref}$ is the characteristic velocity induced by Marangoni stresses due to the temperature gradient.

The governing equations for the velocity, pressure (3.6) and temperature fields (3.10), as well as the boundary conditions (3.13) and (3.14) can be rewritten in dimensionless form:

$$\boldsymbol{\nabla}\widetilde{p} = \boldsymbol{\nabla}^2\widetilde{\mathbf{u}}, \tag{4.3}$$

$$\boldsymbol{\nabla}\cdot\widetilde{\mathbf{u}} = 0 \tag{4.4}$$

$$\boldsymbol{\nabla}^2\widetilde{T} = \frac{\delta(|\widetilde{\mathbf{r}} - \widetilde{\mathbf{r}}_0|)}{|\widetilde{\mathbf{r}} - \widetilde{\mathbf{r}}_0|^2}\ , \tag{4.5}$$

$$-\boldsymbol{\nabla}\widetilde{T}\cdot\mathbf{n} = \mathrm{Bi}\,\widetilde{T}\ , \tag{4.6}$$

$$\mathbf{t}\cdot\widetilde{\boldsymbol{\pi}}\cdot\mathbf{n} = \mathbf{t}\cdot\boldsymbol{\nabla}_{\rm s}\widetilde{T}\ , \tag{4.7}$$

where $\mathrm{Bi} = ha/k_{\rm w}$ is the Biot number. The tildes on top of the dimensionless variables will be omitted in the following sections; henceforward, all variables are dimensionless unless otherwise noted.

4.2. *Temperature field*

The solution to equation (4.5) is obtained via separation of variables. Because the equation is linear, the solution can be written as the sum of the Green's function of the Laplacian with a singularity at $\mathbf{r_0}$, and a continuous function that can be developed in Legendre polynomials. The problem is assumed to be axisymmetric and, in the spherical coordinate system defined in Figure 1, the solution to the heat problem can be written as the following summation:

$$T(r,\theta) = \frac{1}{(r^2+1-2r\cos\theta)^{\frac{1}{2}}} + \sum_{n=0}^{\infty} c_n r^n P_n(\cos\theta) \tag{4.8}$$

where P_n is the Legendre polynomial of order n.

By introducing (4.8) into the boundary condition (4.6), the coefficients, c_n, of the series can be directly identified and evaluated as

$$c_n = \frac{1-2\mathrm{Bi}}{2(n+\mathrm{Bi})}\ . \tag{4.9}$$

Details on this derivation can be found in Appendix A.

4.3. *Velocity field*

For axisymmetric flows, the solution to the Stokes problem can be found in terms of the Stokes' streamfunction ψ (Happel & Brenner (1973)). The velocity field can be extracted from the the streamfunction using the following relations in spherical coordinates:

$$u_r = -\frac{1}{r^2\sin\theta}\frac{\partial\psi}{\partial\theta}\ , \qquad u_\theta = \frac{1}{r\sin\theta}\frac{\partial\psi}{\partial r}\ . \tag{4.10}$$

In spherical coordinates, Stokes equations (3.6) become

$$E^2\left(E^2\psi\right) = 0\ , \tag{4.11}$$

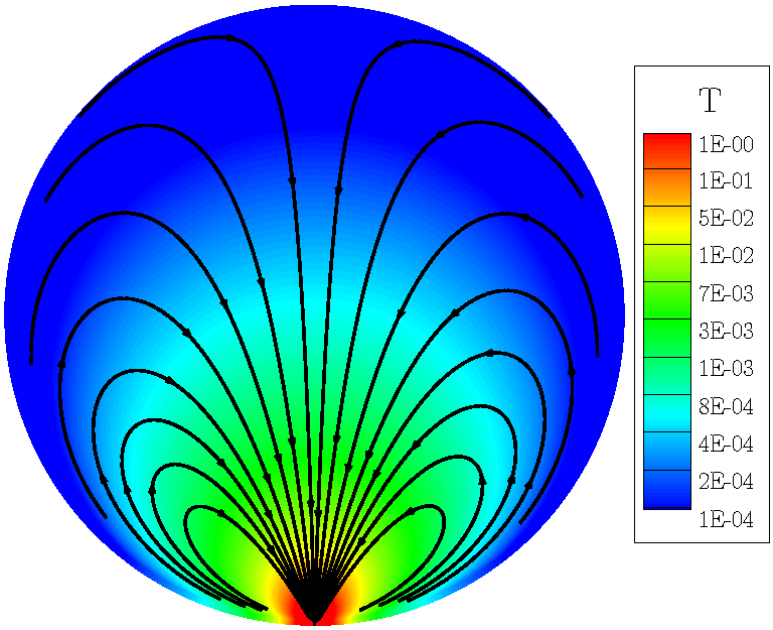

FIGURE 5. Analytic solution of the temperature field and corresponding streamlines. The colormap represents the dimensionless analytical temperature field for Bi = 800 and the black arrows represent the streamlines of the flow in the centerplane defined by $\varphi = 0$. The analytical solution is computed using $n = 100$ terms in the expansion.

where

$$E^2 \equiv \frac{\partial^2}{\partial r^2} + \frac{\sin\theta}{r^2}\frac{\partial}{\partial\theta}\left(\frac{1}{\sin\theta}\frac{\partial}{\partial\theta}\right) \ . \tag{4.12}$$

Using separation of variables, the solution to equation (4.11) can be written as the following series:

$$\psi(r,\theta) = \sum_{n=2}^{\infty}\left(R_n r^n + S_n r^{-n+1} + T_n r^{n+2} + U_n r^{-n+3}\right) C_n^{-1/2}(\cos\theta) \ , \tag{4.13}$$

where $C_n^{-1/2}$ is the Gegenbauer polynomial of order n and degree $-1/2$ defined as

$$C_n^{-1/2}(\cos\theta) = \frac{1}{2n-1}\left[P_{n-2}(\cos\theta) - P_n(\cos\theta)\right] \quad \text{for} \quad n \geq 2 \ . \tag{4.14}$$

Details on the derivation of the solution to equation (4.11) may be found in Happel & Brenner (1973). The streamfunction (4.13) is then introduced in the boundary condition for the Stokes flow (4.7) using (4.10), which takes the following form in spherical coordinates:

$$r\frac{\partial}{\partial r}\left(\frac{u_\theta}{r}\right) + \frac{1}{r}\frac{\partial u_r}{\partial\theta} = -\left.\frac{\partial T}{\partial\theta}\right|_{r=a} \ . \tag{4.15}$$

Identifying the coefficients P_n, Q_n, R_n and S_n in equation (4.13) yields an analytical

expression for the streamfunction

$$\psi(r,\theta) = -\frac{1}{8}(1-r^2)\Bigg[1 + r\cos\theta - \frac{1-r^2}{(r^2+1-2r\cos\theta)^{1/2}} + \sum_{n=2}^{\infty} \frac{(n-1)-(2n-1)\mathrm{Bi}}{(2n-1)((n-1)+\mathrm{Bi})} r^n \left(P_{n-2}(\cos\theta) - P_n(\cos\theta)\right)\Bigg]. \quad (4.16)$$

Details on this derivation can also be found in appendix A. Using equations (4.8) and (4.16), the temperature field and streamfunction can be easily computed. Figure 5 shows the temperature field (4.8) and the streamlines (4.16). The convergence of the sums in the expressions for the temperature field and the streamfunction in equations (4.8,4.16) is dependent on the Biot number, Bi. For higher values of Bi, more terms need to be computed in order to accurately approximate the solution. From the form of the coefficients, we expect the number of terms required to increase linearly with Bi. Finally, the velocity field components, u_r and u_θ, can be deduced from equation (4.16) using equations (4.10).

5. Experimental results and validation of the model

Using the experimental setup described in §2, data was collected for a variety of heat fluxes and drop sizes. The velocity of the flow at different locations was determined by tracking particles. Following this procedure, details of the fluid flow inside the droplet were experimentally reconstructed and compared to the analytical solution developed in §4.3.

5.1. *Optical correction for spherical droplet*

In order to compare the experimentally observed flow field to the analytical solution, we need to correct the observed particle displacements for the optical deformation induced by the fluid droplet itself. The image plane from the midsection of the droplet is focused on the CCD chip of the high-speed camera through the optical system (see Figure 2). However, the hemispherical droplet of water acts as an additional lens between the midsection of the droplet and the optical system (see Figure 6). Applying the Snell-Descartes law (e.g. Halliday *et al.* 2005) to light rays close to the optical axis, the system is found to be stigmatic to the first order and the image of an object $M(0,r)$ in the midsection appears at the point $M'(p',r')$ (see Figure 6) such that

$$p' = g(r) = -\frac{n_{\mathrm{water}}}{n_{air}} r \sin\left[\arcsin r - \arcsin\left(\frac{n_{\mathrm{water}}}{n_{\mathrm{air}}} r\right)\right], \quad (5.1)$$

$$r' = f(r) = \frac{n_{\mathrm{water}}}{n_{air}} r \cos\left[\arcsin r - \arcsin\left(\frac{n_{\mathrm{water}}}{n_{\mathrm{air}}} r\right)\right], \quad (5.2)$$

where r is the distance from the object to the optical axis (recall that lengths have been scaled by the drop radius), r' the distance from the image to the optical axis, p' the distance from the image to the midsection plane of the droplet, n_{water} the index of refraction of water and n_{air} the index of refraction of air. The optical distortion increases with distance from the optical axis. When applied to the raw data, this analysis provides a correction of approximately 17% (of the radius) for $r = 0.65$, which is the upper limit of our recorded data.

5.2. *Comparison between experimental and analytical results*

To compare the analytical solution of the flow field to the experiment, the velocity profile along the x-axis was measured by tracking particles in the focal plane whose trajectories

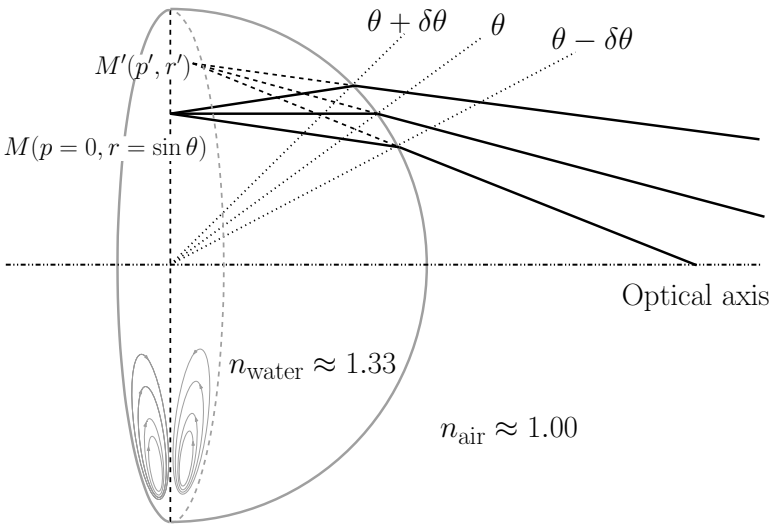

FIGURE 6. Schematic ray-tracing diagram of the geometrical optics for a spherical liquid lens.

	a in mm	Φ_s in J s^{-1}	ΔT_{ref} in K	u_{ref} in m s^{-1}
Experiment 1	0.534	0.0139	3.51	0.54
Experiment 2	0.681	0.0453	8.97	1.39
Experiment 3	0.664	0.0657	13.34	2.06

TABLE 3. Summary of the experimental parameters.

remained close to the x-axis, defined by $\theta = 0$ in spherical coordinates (see Figure 1). The observed position x' of the particle along the axis and its velocity $|\mathbf{u}'|$ were recorded and the real position $x = r$ along the x-axis and velocity $|\mathbf{u}| \approx |u_x|$ were deduced by correcting for optical deformation as described in §5.1: $x = f^{-1}(x')$ and $|\mathbf{u}| = \frac{\mathrm{d}}{\mathrm{dx}} f^{-1}(x')|\mathbf{u}'|$. Several experiments were performed for different magnitudes of the heat source, Φ_s, as summarized in Table 3. The heat flux, Φ_s, was evaluated by measuring the rate of change of the radius of the droplet, which is related to the evaporation loss. Assuming that the bulk of the energy transfer was used in the phase transition, the heat flux is approximated as $\Phi_s \approx 4\pi a^2 \frac{da}{dt} \rho L_v$. The radius of the droplet was roughly half a millimeter in all three experiments. The heat source intensity on the other hand varied significantly between the different experiments (see Table 3). The velocities measured inside the droplets were nondimensionalized using the scaling described in equation (4.2).

Figure 7 shows the dimensionless flow velocities from all three experiments measured along the x-axis and Figure 8 represents the experimentally observed particle pathlines plotted on top of the streamfunction as computed for Bi = 800. Streamlines were recorded experimentally by tracking one particle over an extended period of time. The different sets of data shown in Figure 7 all collapse onto one curve as anticipated, supporting our scaling. This confirms that, in the low Reynolds number and low Péclet number regime, the internal dynamics and heat transfer of the droplet depend on only one dimensionless parameter, the Biot number. Also, as predicted by the model, the velocity is observed to increase rapidly close to the heat source. The only parameter that is not explicitly known in the experiment is the effective heat transfer coefficient, h, which appears in the Biot number. To calculate the analytic velocity profile in Figure 7, we first computed a family

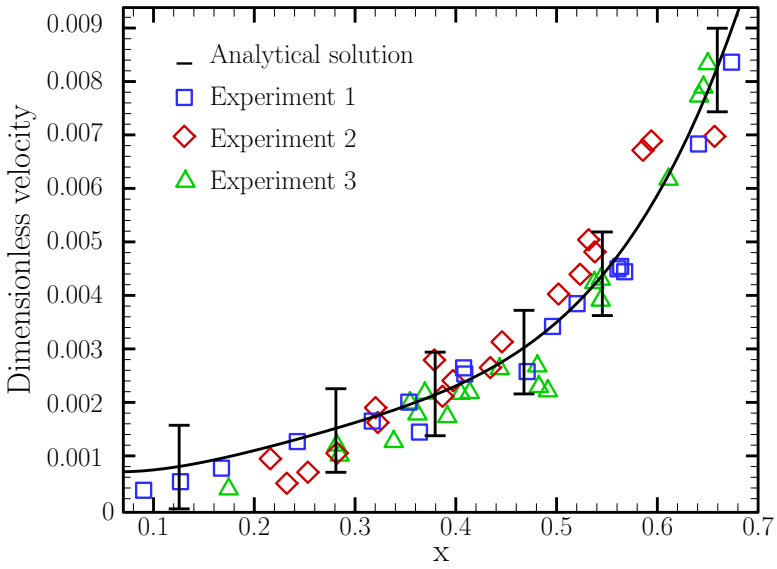

FIGURE 7. Analytical and experimental velocity profile, $|\mathbf{u}|$. The spatial variable x represents the dimensionless coordinate along the x-axis: $x = 0$ lies at the center of the droplet, $x = 1$ lies at the contact point. The black line represents the analytic velocity profile in the drop for Bi = 800. Different symbols correspond to three sets of data with heat sources of different intensity. Error bars give an estimate of the error in measuring the velocity of a particle by extracting the position of its centroid in successive frames and hence are a reflection of the resolution of the image.

of profiles along x, each profile corresponding to a different Bi, and fit the data by minimizing the error between the analytical solution and the experimental data. The fitted Biot number has a value of Bi = 800, which corresponds to a generalized heat transfer coefficient of $h \approx 7.1 \times 10^5$ W m^{-2}K^{-1}. In comparison, the heat transfer coefficient for a sphere in quiescent air cooled only by diffusion is on the order of 10^2 W m^{-2}K^{-1}, corresponding to the small Biot number limit in which only small temperature gradients are expected inside the sphere. This suggests that, in our case, evaporation is the dominant form of heat transfer from the droplet to the surrounding air and thus $h \approx h_e$†. However, even for heat transfer in systems involving phase changes (which can easily achieve h's on the order of 10^4 or 10^5 W m^{-2}K^{-1}), our value is quite high and we believe that, in neglecting convective transport (i.e. assuming small Péclet number everywhere), we are perhaps overestimating h. While our results are correct to first order, the addition of convective effects would tend to smooth out the temperature gradient near the singularity, lowering the effective heat transfer coefficient. A quantitative analysis of the first order effects of finite Pe is included in Appendix D.

6. Discussion

In conclusion, we have observed convective structures inside water droplets sitting on superhydrophobic surfaces. A physical model has been proposed, suggesting that these structures arise due to thermocapillary-driven Marangoni convection. Because the Reynolds number and Péclet number are small and viscous dissipation is negligible in the

† This is consistent with our heat flux estimations, since we have chosen $\Phi_s \approx \iint \phi_{\text{evaporation}}\, dS$.

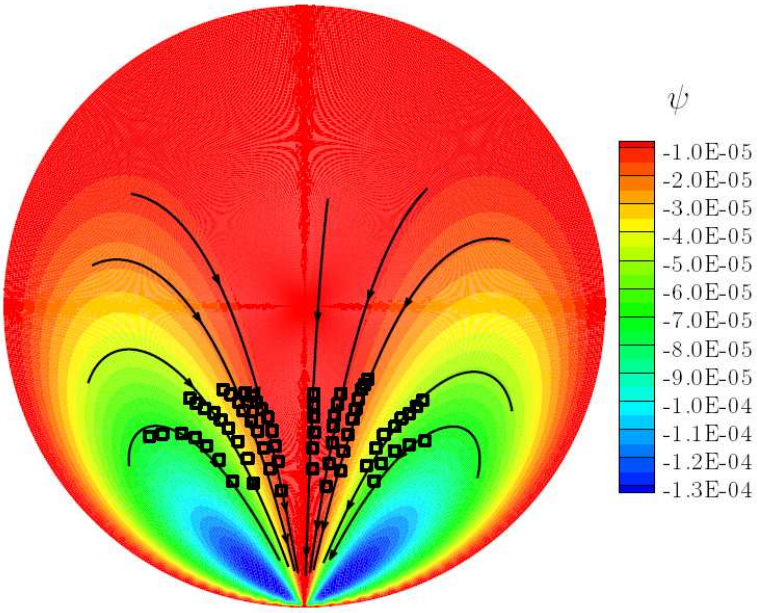

FIGURE 8. Analytical and experimental streamlines. The colormap represents the analytical streamfunction; black lines represent particular streamlines computed analytically; black squares represent experimentally recorded particle trajectories. The analytical solution is computed using $n = 100$ terms in the expansion.

energy balance, the heat transfer and fluid momentum problems decouple. It is then possible to find a solution analytically in terms of Gegenbauer polynomials. This solution has the form of a toroidal vortex and compares favorably with experimental measurements of particle pathlines inside the drop. By matching the Biot number from experimental observations to the numerical simulation, we are able to estimate the effective heat transfer coefficient $h \approx 7.1 \times 10^5$ W m^{-2}K^{-1} for droplets sitting on hot hydrophobic surfaces.

It may come as some surprise that, in our physical model, the dynamics of the system depends on only one dimensionless parameter, Bi, whereas a standard dimensional analysis would predict four relevant dimensionless groups: the Reynolds number, Re, the Péclet number, Pe, the Biot number, Bi and the Marangoni number, $\mathrm{Ma} = \alpha a \Delta T / \kappa \mu$. However, recall that as a first approximation, both the Reynolds number and the Péclet are assumed to be small. Since $\mathrm{Pe} = \mathrm{Re} \cdot \mathrm{Pr}$, the Reynolds number and the Péclet number cannot be varied independently without changing the material properties of the fluid. This assumption reduces the number of independent dimensionless groups to two. Furthermore, the governing equations are linear in velocity thus the velocity scale may be chosen to eliminate a third dimensionless group. By using the characteristic Marangoni velocity, $\alpha \Phi_\mathrm{s} / \mu k_\mathrm{w}$, as a reference velocity, the Marangoni number can be eliminated from the dimensionless governing equations. Thus, the small Reynolds number assumption combined with the linear structure of the governing equations leaves only one dimensionless parameter, Bi. Note however that the *dimensional* velocities still scale linearly with the Marangoni number.

Furthermore, the analysis could be extended to include the influence of finite Pe and Re by including a small Pe and Re perturbation about the base state computed herein. This introduces a weak coupling between the fluid flow and the heat transfer, ultimately yielding a dimensionless heat transfer correlation function for the Biot (or Nusselt) num-

ber as a function of Re, Pe and Ma. The first order effects of finite Péclet number are described in Appendix D, however a detailed analysis is beyond the scope of the present manuscript.

Finally, it is notable that, in addition to heat transfer applications discussed herein, the Marangoni convection discussed in this work may be exploited to enhance micromixing in fluid droplets (Darhuber *et al.* 2004) and possibly as original microbiological assays (Chang & Velev 2006).

The authors gratefully acknowledge the support of the National Science Foundation (CTS-0456092 and CCF-0323672).

REFERENCES

Biance, A.-L., Clanet, C. & Quéré, D. 2003 Leidenfrost drops. *Physics of Fluids* **15** (6), 1632.

Bico, J., Marzolin, C. & Quéré, D. 1999 Pearl drops. *Europhys. Lett.* **47**, 220 – 226.

Chandrasekhar, S. 1961 *Hydrodynamic and hydromagnetic stability*. Oxford: Clarendon press.

Chang, S. T. & Velev, O. D. 2006 Evaporation-induced particle microseparations inside droplets floating on a chip. *Langmuir* **22**, 1459 – 1468.

Daniel, S., Chaudhury, M. K. & Chen, J. C. 2001 Fast drop movements resulting from the phase change on a gradient surface. *Science* **291** (5504), 633 – 636.

Darhuber, A. A., Chen, J. Z., Davis, J. M. & Troian, S. M. 2004 A study of mixing in thermocapillary flows on micropatterned surfaces. *Phil. Trans. R. Soc. Lond. A* **362**, 1037 – 1058.

Davis, S. H. 1987 Thermocapillary instabilities. *Ann. Rev. Fluid Mech.* **19**, 403.

Deegan, R. D., Bakajin, O., Dupont, T. F., Huber, G., Nagel, S. R. & Witten, T. A. 1997 Capillary flow as the cause of ring stains from dried liquid drops. *Nature* **389**, 827 – 829.

Erb, R. A. & Thelen, E. 1965 Promoting permanent dropwise condensation. *Ind. Eng. Chem.* **57** (10), 49 – 52.

Gao, L. & McCarthy, T. J. 2006 A perfectly hydrophobic surface. *J. Am. Chem. Soc.* **128**, 9052–9053.

Halliday, D., Resnick, R. & Walker, J. 2005 *Fundamentals of physics, seventh edition*. New York: Wiley.

Happel, J. & Brenner, H. 1973 *Low Reynolds number hydrodynamics*. Leyden: Noordhoff int. publ.

He, B., Patankar, N. & J, J. L. 2003 Multiple equilibrium droplet shapes and design criterion for rough hydrophobic surfaces. *Langmuir* **19**, 4999–5003.

Hu, H. & Larson, R. G. 2005 Analysis of the effects of marangoni stresses on the microflow in an evaporating sessile droplet. *Langmuir* **21**, 3972 – 3980.

Incropera, F. P. & deWitt, D. P. 2002 *Fundamentals of heat and mass transfer, fifth edition*. New York: Wiley.

Jia, W. & Qiu, H. 2002 Fringe probing of an evaporating microdroplet on a hot surface. *Int. J. Heat and Mass Trans.* **45**, 4141–4150.

Kandlikar, S. G. 2001 A theoretical model to predict pool boiling chf incorporating effects of contact angle and orientation. *ASME Journal of Heat Transfer* **123**, 1071–1079.

Krupenkin, T. N., Taylor, J. A., Schneider, T. M. & Yang, S. 2004 From rolling ball to complete wetting: The dynamic tuning of liquids on nanostructured surfaces. *Langmuir* **20**, 3824–3827.

Lafuma, A. & Quéré, D. 2003 Superhydrophobic states. *Nature Materials* **2** (7), 457–460.

Lau, K. K. S., Bico, J., Teo, K. B. K., Chhowalla, M., Amaratunga, G. A. J., Milne, W. I., McKinley, G. H. & Gleason, K. K. 2003 Superhydrophobic carbon nanotube forests. *Nano Lett.* **3 (12)**, 1701–1705.

Mahadevan, L. & Pomeau, Y. 1999 Rolling droplets. *Pjys. Fluids* **11** (9), 2449–2453.

Makino, K., Michiyoshi, I., Sakamoto, K. & Hojo, K. 1984 The behaviour of a water droplet on heated surfaces. *Int. J. Heat. Mass Transfer* **27 (5)**, 781–791.

Marangoni, C. 1865 On the expansion of a drop of liquid floating on the surface of another liquid. Tipographia dei fratelli Fusi, Pavia.

McHale, G., Aqil, S., Shirtcliffe, N. J., Newton, M. I. & Erbil, H. Y. 2005 Analysis of droplet evaporation on a superhydrophobic surface. *Langmuir* **21** (24), 11053–11060.

Onda, T., Shibuichi, S., Satoh, N. & Tsujii, K. 1996 Super-water-repellent fractal surfaces. *Langmuir* **12**, 2125.

Otten, A. & Herminghaus, S. 2004 How plants keep dry: A physicists point of view. *Langmuir* **20**, 2405–2408.

Qiao, Y. M. & Chandra, S. 1997 Experiments on adding surfactant to water drops boiling on a hot surface. *Proc. R. Soc. Lond. A* **453**, 673 – 689.

Quéré, D. 2002 Fakir droplets (news & views). *Nature Materials* **1**, 14 – 15.

Quéré, D. 2003 Rough ideas on wetting. *Physica A* **313**, 32–46.

Sadhal, S. S. & Plesset, M. S. 1979 Effect of solid properties and contact angle dropwise condensation and evaporation. *J. Heat Transfer* **101**, 48–54.

Schatz, M. F. & Neitzel, G. P. 2001 Experiments on thermocapillary instabilities. *Ann. Rev. Fluid Mech.* **33**, 93 – 127.

Schmidt, E., Schurig, W. & Sellschopp, W. 1930 Versuche über die kondensation von wasserdampf in film- und tropfenform. *Techn. Mech. u. Thermodynam.* **1**, 53.

Scriven, L. E. & Sternling, C. V. 1964 On cellular convection driven by surface-tension gradients: effects of mean surface tension and surface viscosity. *J. Fluid Mech.* **19**, 321340.

Subramanian, R. S. & Balasubramaniam, R. 2001 *The motion of bubbles and drops in reduced gravity*. Cambridge: Cambridge university press.

Thomas, O. C., Cavicchi, R. E. & Tarlov, M. 2003 Effect of surface wettability on fast transient microboiling behavior. *Langmuir* **19** (15), 6168 – 6177.

Wang, C. H. & Dhir, V. K. 1993 Effect of surface wettability on active nucleation site density during pool boiling of water on a vertical surface. *Journal of Heat Transfer* **115**, 659.

Wenzel, R. N. 1936 Resistance of solid surfaces to wetting by water. *Ind. Eng. Chem.* **28** (8), 988.

Zhai, L., Cebeci, F. C., Cohen, R. E. & Rubner, M. F. 2004 Stable superhydrophobic coatings from polyelectrolyte multilayers. *Nanolet.* **4**, 1349–1353.

Zhao, N., Xu, J., Xie, Q., Weng, L., Guo, X., Zhang, X. & Shi, L. 2005 Fabrication of biomimetic superhydrophobic coating with a micro-nano-binary structure. *Macromolecular Rapid Communications* **26**, 1075 – 1080.

Appendix A. Derivation of the analytical solution

In this appendix we present the detailed derivation of the analytical solution. The boundary condition (4.5) takes the following dimensionless form:

$$-\frac{\partial}{\partial r}T(r,\theta)\bigg|_{r=1} = \mathrm{Bi}\ T(1,\theta). \tag{A 1}$$

The *a priori* expression for the temperature (4.8) is differentiated with respect to r

$$\frac{\partial}{\partial r}T(r,\theta)\bigg|_{r=1} = -\frac{1-\cos\theta}{(2-2\cos\theta)^{\frac{3}{2}}} + \sum_{n=0}^{\infty} n c_n P_n(\cos\theta). \tag{A 2}$$

This expression (A 2) is introduced in the boundary condition (A 1) and yields the following relationship:

$$\sum_{n=0}^{\infty}(n+\mathrm{Bi})c_n P_n(\cos\theta) = \frac{1-2\mathrm{Bi}}{2(2-2\cos\theta)^{\frac{1}{2}}}. \tag{A 3}$$

Using the identity

$$\frac{1}{(r^2+1-2r\cos\theta)^{\frac{1}{2}}} = \sum_{n=0}^{\infty} r^n P_n(\cos\theta) \tag{A 4}$$

at $r=1$ and the fact that the Legendre representation is unique, the coefficients c_n can be determined

$$c_n = \frac{1-\mathrm{Bi}}{2(n+\mathrm{Bi})} \ . \tag{A 5}$$

Expanding the streamfunction in Gegenbauer polynomials (4.13) in equation (4.10) and using the identities from Appendix B yields the following series expansion for the radial velocity:

$$u_r = \sum_{n=2}^{n=\infty} \left(R_n r^{n-2} + S_n r^{-(n+1)} + T_n r^n + U_n r^{-(n-1)} \right) \ P_{n-1}(\cos\theta). \tag{A 6}$$

Since u_r has to be bounded at $r=0$, the coefficients S_n and U_n must vanish. Also, the radial velocity must vanish at the interface $r=1$ for the droplet to remain spherical, thus $T_n = -R_n$. Hence the expansion (4.13) of the streamfunction can be rewritten in a simpler form

$$\psi(r,\theta) = \sum_{n=2}^{\infty} R_n \left(r^n - r^{n+2}\right) C_n^{-1/2}(\cos\theta) \ . \tag{A 7}$$

The expression for the temperature field (4.8) and for the stream function (A 7) are introduced in the tangential stress boundary condition (4.7):

$$\sum_{n=2}^{\infty} 2(1-2n) R_n \ \frac{C_n^{-1/2}(\cos\theta)}{\sin\theta} = \frac{\sin\theta}{(2-2\cos\theta)^{\frac{3}{2}}} + \sum_{n=2}^{\infty} n(n-1) c_{n-1} \frac{C_n^{-1/2}(\cos\theta)}{\sin\theta} \ . \tag{A 8}$$

Using the identity

$$\frac{\sin\theta}{(2-2\cos\theta)^{\frac{3}{2}}} = \sum_{n=2}^{\infty} n(n-1) \frac{C_n^{-1/2}(\cos\theta)}{\sin\theta} \tag{A 9}$$

the tangential stress boundary condition yields the equation

$$\sum_{n=2}^{\infty} 2R_n(2n-1) \ C_n^{-1/2}(\cos\theta) = -\sum_{n=2}^{\infty} (1+c_{n-1})(n-1)n \ C_n^{-1/2}(\cos\theta) \ . \tag{A 10}$$

Thus, $R_n = -\frac{n(n-1)}{2(2n-1)}(1+c_{n-1}) \ , \forall \ n \geq 2$. Rearranging the different terms, in order to isolate the singularity at $\mathbf{r_0}$ yields the final expression for the stream velocity (4.16).

Appendix B. Properties of Gegenbauer polynomials

$$\frac{d \ C_n^{-1/2}(\cos\theta)}{d\theta} = \sin\theta \ P_{n-1}(\cos\theta) \ ,$$
$$\frac{d \ P_{n-1}(\cos\theta)}{d\theta} = -\frac{n(n-1) C_n^{-1/2}(\cos\theta)}{\sin\theta} \ .$$

Appendix C. Validity of the point heat source approximation

In this appendix, we investigate the validity of the point heat source assumption. As droplet size decreases, the radius ℓ of the contact region between the droplet and the substrate decreases rapidly as suggested by the scaling giving in equation (3.3) of §3.1. In our experiments, the ratio between the radius of the contact region and the radius of the droplet is on the order of $\ell/a \approx 10\%$ (see Figure 3). To determine whether the finite extent of the heat source in the experiments has a significant impact on the observed flows, we model the source as a distributed heat source rather than as a singular point. The governing equations for the heat transport problem (3.10, 3.13) are replaced by

$$k_{\mathrm{w}} \boldsymbol{\nabla}^2 T^\alpha = 0 \ , \tag{C 1}$$

$$-k_{\mathrm{w}} \boldsymbol{\nabla} T^\alpha \cdot \mathbf{n} = h(T^\alpha - T_0) + \frac{\Phi_{\mathrm{s}}}{4\pi a^2} f^\alpha(\cos\theta) \ , \tag{C 2}$$

which can be written in nondimensional form as

$$\boldsymbol{\nabla}^2 T^\alpha = 0 \ , \tag{C 3}$$

$$-\boldsymbol{\nabla} T^\alpha \cdot \mathbf{n} = \mathrm{Bi}\ T^\alpha + f^\alpha(\cos\theta) \ . \tag{C 4}$$

The function $f^\alpha(\cos\theta)$ characterizes the distribution of the heat source, subject to the normalization constraint

$$\int_0^\pi f^\alpha(\cos\theta)\sin\theta \ d\theta = 2 \ . \tag{C 5}$$

Here we consider a sequence of functions f^α defined as follows:

$$f^\alpha(\cos\theta) = \begin{cases} \frac{6(\cos\theta - \cos\alpha)^2}{(1-\cos\alpha)^3} & 0 \le \theta \le \alpha, \\ 0 & \alpha \le \theta \le \pi \end{cases}$$

where α characterizes the area over which the heat source is distributed. As α decreases, this sequence of functions converges to a delta function.

A derivation similar to the one presented in Appendix A yields the following expressions for the temperature field and the streamfunction:

$$T^\alpha(r,\theta) = \sum_{n=0}^{\infty} \frac{f_n^\alpha}{n+\mathrm{Bi}} r^n P_n(\cos\theta) \ , \tag{C 6}$$

$$\psi^\alpha(r,\theta) = \sum_{n=2}^{\infty} -\frac{n(n-1)f_{n-1}^\alpha}{2(2n-1)(n-1+\mathrm{Bi})} \left(r^n - r^{n+2}\right) C_n^{-1/2}(\cos\theta) \ , \tag{C 7}$$

where

$$f_n^\alpha = \frac{2n+1}{2} \int_{-1}^{1} f^\alpha(x) P_n(x) dx \ . \tag{C 8}$$

Figure 9(a) shows the convergence of the solution T^α for a distributed heat source to the solution T for a point heat source as α goes to zero. Figure 9(b) shows the magnitude of the flow velocity along the x-axis within the region of the droplet that can be observed experimentally (see figure 7). The velocity profile for a heat source distributed over 20% of the radius is already very close to that of a point heat source and, not surprisingly, the convergence is even more pronounced for a source distributed over 10% of the radius. As expected the distribution of the heat source only affects the solution of the flow in the vicinity of the contact region. In the present study, our model is always compared to experimental data in a region of the droplet sufficiently far from the contact point (see figure 9b) and hence, the heat source can be safely represented as a point source.

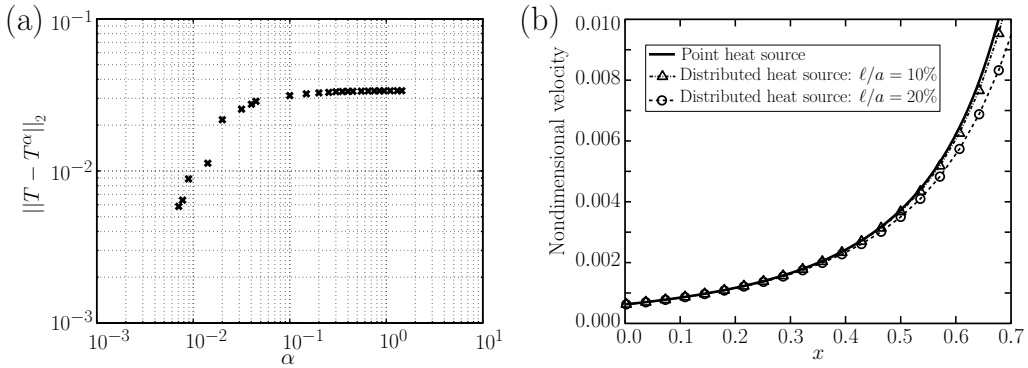

FIGURE 9. a) Error $\|T - T^\alpha\|_2$ as a function of α showing the convergence of the sequence T^α to the point heat source solution T. b) Velocity profile $|\mathbf{u}|$ along the x-axis for the point heat source solution and for distributed heat source solutions with $\ell/a = 10\%$ and 20%.

Appendix D. Effect of finite Péclet number

Here, we investigate the first-order effect of heat advection on the steady state temperature, pressure and velocity fields. For a finite Péclet number, the governing equations in nondimensional form can be written as

$$\boldsymbol{\nabla}^2 T - \frac{\delta(|\mathbf{r} - \mathbf{r}_0|)}{|\mathbf{r} - \mathbf{r}_0|^2} = \mathrm{Pe}\ \mathbf{u} \cdot \boldsymbol{\nabla} T, \tag{D 1}$$

$$\boldsymbol{\nabla}^2 \mathbf{u} = \boldsymbol{\nabla} p\ , \tag{D 2}$$

$$\boldsymbol{\nabla} \cdot \mathbf{u} = 0\ , \tag{D 3}$$

$$-\boldsymbol{\nabla} T \cdot \mathbf{n} = \mathrm{Bi}\, T\ , \tag{D 4}$$

$$\mathbf{t} \cdot \boldsymbol{\pi} \cdot \mathbf{n} = \mathbf{t} \cdot \boldsymbol{\nabla}_\mathrm{s} T\ . \tag{D 5}$$

The fields are each split into two terms: $\mathbf{u} = \mathbf{u}_0 + \mathbf{u}_1$, $T = T_0 + T_1$ and $p = p_0 + p_1$, where the subscript "0" represents the known analytical solution to the zero Péclet number problem (4.8 and 4.16) and the subscript "1" represents the perturbation fields due to the nonlinear advection term for finite Péclet number. This splitting scheme is introduced in (D 1), (D 2), (D 3), (D 4) and (D 5). The solution $(\mathbf{u}_0, p_0, T_0)$ to the linear system with a point heat source is substracted from the finite Péclet number system, leading to a set of equations for the perturbation field $(\mathbf{u}_1, p_1, T_1)$. These equations are discretized using finite differences and the full nonlinear system is solved using the following iteration scheme

$$\boldsymbol{\nabla}^2 T_1^{n+1} - \mathrm{Pe}\ (\mathbf{u}_0 + \mathbf{u}_1^n) \cdot \boldsymbol{\nabla} T_1^{n+1} = \mathrm{Pe}\ (\mathbf{u}_0 + \mathbf{u}_1^n) \cdot \boldsymbol{\nabla} T_0, \tag{D 6}$$

$$\boldsymbol{\nabla}^2 \mathbf{u}_1^{n+1} = \boldsymbol{\nabla} p_1^{n+1}\ , \tag{D 7}$$

$$\boldsymbol{\nabla} \cdot \mathbf{u}_1^{n+1} = 0\ , \tag{D 8}$$

$$-\boldsymbol{\nabla} T_1^{n+1} \cdot \mathbf{n} = \mathrm{Bi}\, T_1^{n+1}\ , \tag{D 9}$$

$$\mathbf{t} \cdot \boldsymbol{\pi}_1^{n+1} \cdot \mathbf{n} = \mathbf{t} \cdot \boldsymbol{\nabla}_\mathrm{s} T_1^{n+1}\ . \tag{D 10}$$

The iteration procedure is stopped once the convergence criterion $\|\mathbf{u}_1^{n+1} - \mathbf{u}_1^n\|_2 \leq \epsilon$ is satisfied.

When the advection term is included, cool water is advected downwards through the center of the droplet towards the contact point, which lowers the temperature in this

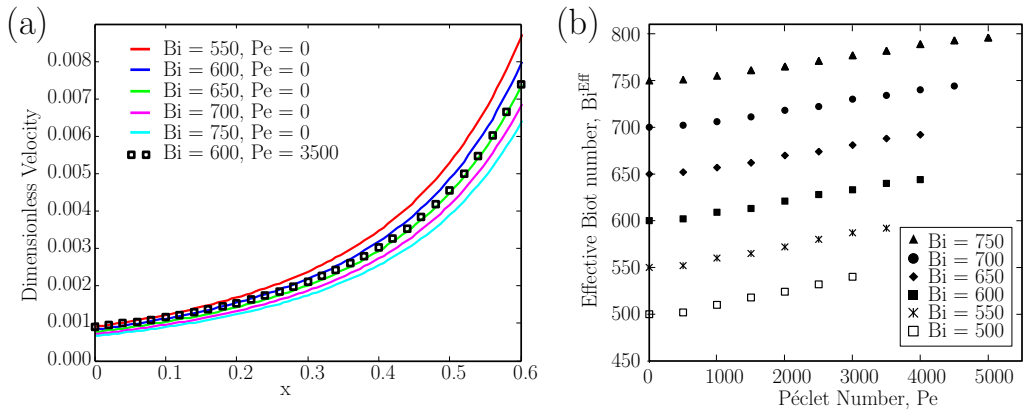

FIGURE 10. (a) Effect of increasing Biot number and increasing Péclet number on the velocity along the x-axis. (b) "Effective Biot number" for which the velocity profile of the numerical solution along the x-axis best fits the analytical Pe = 0 solution as a function of the Péclet number.

region. Similarly heat is swept away from the contact region and advected to the sides of the droplet, which reduces temperature gradients in the neighborhood of the source. The general effect is to decrease the Marangoni stress at the surface of the droplet and thus, for a given Biot number, we expect to observe smaller velocities. Hence, increasing the Péclet number has a similar effect on the velocity field as increasing the Biot number: both tend to lower the temperature gradient at the surface and as a consequence the Marangoni stress. Therefore, it is expected that for a given Péclet number the Biot number required to fit the experimental data will be lower than the first order estimate in which we neglected heat advection.

This can be seen in Figure 10(a). Consider a velocity profile along the x-axis for a Biot number of Bi = 600 and a Péclet number of Pe = 3500. This velocity profile is almost indistinguishable from the velocity profile for Bi = 650 and Pe = 0. To quantify this feature, we define an "effective Biot number," $\mathrm{Bi}^{\mathrm{Eff}}(\mathrm{Pe})$, which is the Biot number at a given Péclet number that matches the Pe = 0 velocity profile when heat advection is neglected (in this example, $\mathrm{Bi}^{\mathrm{Eff}}(\mathrm{Pe} = 3500) = 650$). It can readily be seen that increasing the Péclet number has a similar influence on the velocity profile as increasing the effective Biot number.

Note that even at a seemingly large Péclet number of Pe = 3500, the heat advection term remains small within most of the volume of the droplet and is only non-negligible in the neighborhood of the contact region. This is because the Péclet number is proportional to the reference velocity, u_{ref}, used in the nondimensionalization, which represents the velocity induced close to the heat source singularity (see Section 4.1). In contrast, the value of the Péclet number computed with the flow velocity measured at the center of the droplet is small as discussed in Section 3.2. Figure 10(b) characterizes the increase in effective Biot number as the Péclet number is increased for a fixed Biot number. The effective Biot number is found by minimizing the error between the velocity profile computed at a given Biot and Péclet number, and the velocity profiles for a given Biot number with no heat advection. As expected, the effective Biot number always increases with increasing Péclet number indicating that, by neglecting heat advection, our lowest order model is likely to overestimate the Biot number and the effective heat transfer coefficient. The severity of the error is illustrated in Figure 10(b) for the parameter

regime where the heat advection terms remain small and the governing equations are only weakly nonlinear.